

Many-beam dynamical simulation for multilayer structures without a superlattice cell

Masahiro Ohtsuka,^{a*} Takashi Yamazaki,^a Iwao Hashimoto^a and Kazuto Watanabe^b

Received 20 June 2008

Accepted 19 December 2008

^aDepartment of Physics, Tokyo University of Science, Tokyo, 162-8601, Japan, and ^bTokyo Metropolitan College of Industrial Technology, Tokyo, 140-0011, Japan. Correspondence e-mail: j1207612@ed.kagu.tus.ac.jp

A many-beam dynamical theory for plan-view high-resolution transmission electron microscopy (HRTEM) images of multilayer systems without the limitation of a superlattice cell is proposed. The accuracy of our method is examined by comparing convergent-beam electron-diffraction calculations of Si(011) and HRTEM calculations of a system of epitaxial Al(100) on GaAs(100). Furthermore, this method is applied to CdSe clusters embedded in MgO, where it is revealed that the relative shift of their crystal-lattice planes produces moiré-like fringes.

© 2009 International Union of Crystallography
Printed in Singapore – all rights reserved

1. Introduction

The ever-decreasing dimensions of devices during the last few decades has necessitated the elucidation of the local properties of the materials used in semiconductor technology as well as the strain induced around the interfaces in heterogeneous systems (Timp, 1988; Hull *et al.*, 2000). Modern devices are rapidly approaching the atomic scale, and their nanoscale behavior has become one of the most active areas of research in materials science. As for heteroepitaxial thin films, the interfacial structure and lattice mismatch at the interface between the film and the substrate play a key role in controlling the epitaxial quality, microstructure and physical properties of the film. However, very few techniques are likely to provide a highly localized and yet accurate analysis.

One technique for the characterization of such nanostructures may be transmission electron microscopy (TEM); TEM has several attractive features and is employed in many different systems for observing different images. In particular, high-resolution TEM (HRTEM) has been successfully used for the structural analysis of many objects. Generally, cross-section TEM is used to investigate the interfacial structures in various heteroepitaxial films (Gao *et al.*, 1999; Jia & Urban, 1999; Jia *et al.*, 2003). However, the interfacial structure information obtained using this technique is limited to one-dimensional space. Plan-view TEM, on the other hand, can provide significant structural information over a large interfacial area, which is necessary for understanding the mechanism of lattice relaxation (Jiang *et al.*, 2007). However, the images obtained by plan-view TEM are not simple functions of the crystal structures and do not always reveal the real projected atomic structures due to a phase effect and lens aberrations. Therefore, HRTEM images must be interpreted carefully and extensive image simulations are required.

Dynamical simulation of electron diffraction is a well known and popular technique; the simulation methods are

classified into two general types, namely, the multislice method (Cowley & Moodie, 1957; Van Dyck, 1980; Ishizuka, 1982; Self, 1982) and the Bloch-wave method (Bethe, 1928; Fujimoto, 1959; Hirsch *et al.*, 1965). The multislice method involves mathematically slicing the specimen along the beam direction. It is based on a convolution calculation and is thus quite flexible. The Bloch-wave method is based on an eigenvalue problem and provides a valuable physical insight into the scattering process.

In order to perform dynamical simulations for defects such as precipitates and heterostructures, the plan-view TEM method is employed and a superlattice cell is generally introduced, because most calculation processes in the two methods are carried out without any change to their algorithms. However, since the superlattice cell is selected such that one lattice parameter is the least common multiple of the other, the superlattice size becomes extremely large, thereby making the calculation very difficult. This is a fundamental limitation in both the Bloch-wave method and the multislice method. In this paper, we expand on the layer-by-layer method (Eaglesham *et al.*, 1989; Rossouw *et al.*, 1991; Al-Khafaji *et al.*, 1992; Wang *et al.*, 1992; Rossouw & Perovic, 1993; Yamazaki *et al.*, 2006) for plan-view TEM of embedded clusters or interfaces to express the dynamical propagation of fast electrons through successive crystal layers by using interface boundary conditions and converting the transmitted waves into incident waves in the next layer. This method enables us to perform HRTEM simulations of a mismatched multilayer film. These films revealed that moiré-like lattice fringes are formed due to the relative shift of the crystal-lattice planes of CdSe clusters embedded in MgO.

2. Theory

The basic concept of the layer-by-layer method using a superlattice cell has been discussed in detail by several authors

(Rossouw *et al.*, 1991; Wang *et al.*, 1992; Yamazaki *et al.*, 2006); therefore, in this paper, we shall only briefly explain the process. When a plane wave illuminates a multilayer structure, as shown in Fig. 1, the incident wave with unit amplitude can be written as

$$\Psi_{\text{inci}}^{(0) \rightarrow (1)}(\mathbf{R}, z) = \exp\left\{i\left[\mathbf{K}_{\parallel}^{(0)} \cdot \mathbf{R} + k_z^{(0)}(\mathbf{K}_{\parallel}^{(0)})z\right]\right\}, \quad (1)$$

where $\mathbf{K}_{\parallel}^{(0)}$ is the transverse (parallel to the surface) component of the incident plane wave in vacuum and $k_z^{(0)}$ is the longitudinal (normal to the surface) component of the incident wavevector in vacuum. The subscript (*i*) denotes the *i*th layer (*i* = 0 represents the vacuum layer). In the Bloch-wave

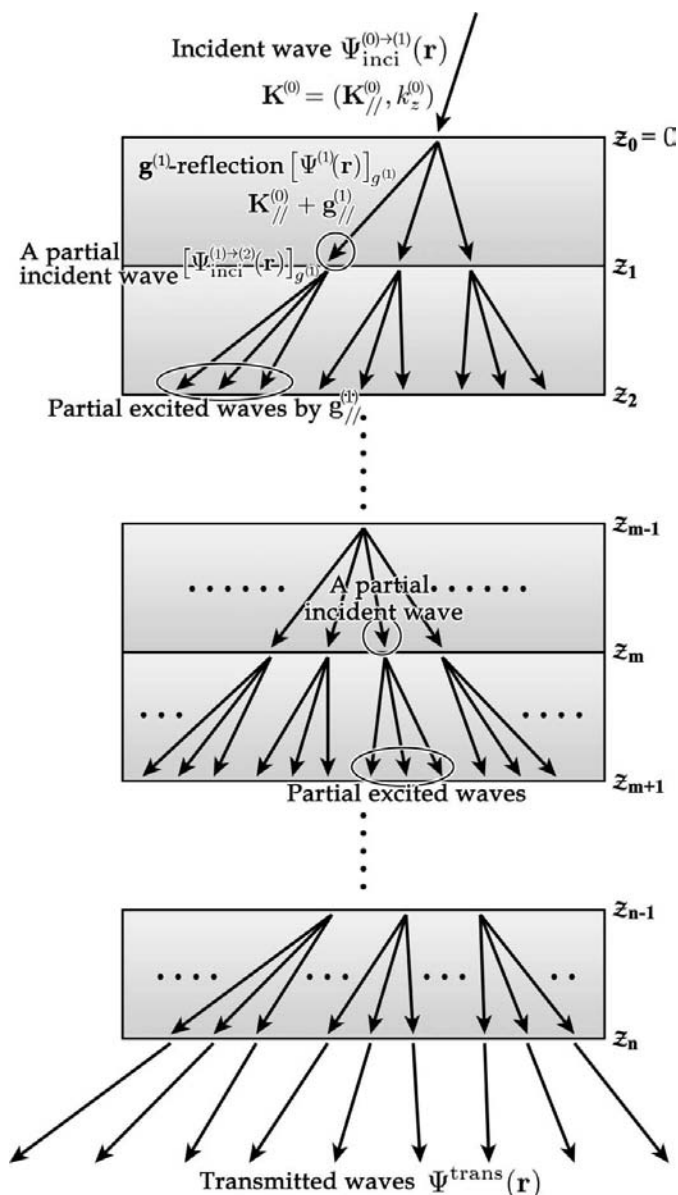


Figure 1
Schematic diagram of an electron propagating through a multilayer structure.

model, the wavefunction formed by an incident wave at $\mathbf{r} = (\mathbf{R}, z)$ in the first layer can be expressed as

$$\Psi^{(1)}(\mathbf{R}, z) = \sum_{g^{(1)}} \sum_j \alpha^{(1),j}(\mathbf{K}_{\parallel}^{(0)}) C_{g^{(1)}}^{(1),j}(\mathbf{K}_{\parallel}^{(0)}) \exp\left[i\left(\mathbf{K}_{\parallel}^{(0)} + \mathbf{g}_{\parallel}^{(1)}\right) \cdot \mathbf{R}\right] \times \exp\left\{i\left[k_z^{(1)}(\mathbf{K}_{\parallel}^{(0)}) + \gamma^{(1),j}(\mathbf{K}_{\parallel}^{(0)}) + g_z^{(1)}\right]z\right\}, \quad (2)$$

where $\alpha^{(1),j}(\mathbf{K}_{\parallel}^{(0)})$ and $\gamma^{(1),j}(\mathbf{K}_{\parallel}^{(0)})$ denote the excitation amplitudes and the eigenvalues for the *j*th branch in the first layer, respectively. $C_{g^{(1)}}^{(1),j}(\mathbf{K}_{\parallel}^{(0)})$ denote the Bloch-wave coefficients for Bragg reflection $\mathbf{g}^{(1)} = (\mathbf{g}_{\parallel}^{(1)}, g_z^{(1)})$. The Bloch-wave coefficients and eigenvalues are determined by solving the fundamental equation including absorption, which can be formulated as

$$\left[\mathbf{K}^2 - (\mathbf{k}^j + \mathbf{g})^2 + iU'_0\right] C_g^j(\mathbf{K}_{\parallel}) + (2me/\hbar^2) \sum_{g \neq h} V_{g-h} C_h^j(\mathbf{K}_{\parallel}) = 0, \quad (3)$$

where $\mathbf{K}^2 = (\mathbf{K}^{(0)})^2 + U_0$, $2meV_{g-h}/\hbar^2 = U_{g-h} + iU'_{g-h}$ and $\mathbf{k}^j = (\mathbf{K}_{\parallel}, k_z + \gamma^j(\mathbf{K}_{\parallel}))$. U_{g-h} and U'_{g-h} denote the Fourier coefficients of the elastic and absorption potentials, *m* denotes the electron rest mass, and *e* denotes the electric charge.

By straightforward approximation, the boundary condition on the entrance surface ($z = z_0 \equiv 0$) gives rise to the matrix form

$$\begin{bmatrix} \alpha^{(1),1}(\mathbf{K}_{\parallel}^{(0)}) \\ \alpha^{(1),2}(\mathbf{K}_{\parallel}^{(0)}) \\ \alpha^{(1),3}(\mathbf{K}_{\parallel}^{(0)}) \\ \vdots \end{bmatrix} = [\tilde{\mathbf{C}}^{(1)}(\mathbf{K}_{\parallel}^{(0)})]^{-1} \cdot \begin{bmatrix} 1 \\ 0 \\ 0 \\ \vdots \end{bmatrix}, \quad (4)$$

where $[\tilde{\mathbf{C}}^{(1)}(\mathbf{K}_{\parallel}^{(0)})]^{-1}$ is the inverse matrix of the eigenvector. The wavefunction in the first layer can be rewritten as

$$\Psi^{(1)}(\mathbf{R}, z) = \sum_{g^{(1)}} \left(\sum_j \alpha^{(1),j}(\mathbf{K}_{\parallel}^{(0)}) C_{g^{(1)}}^{(1),j}(\mathbf{K}_{\parallel}^{(0)}) \times \exp\left\{i\left[k_z^{(1)}(\mathbf{K}_{\parallel}^{(0)}) + \gamma^{(1),j}(\mathbf{K}_{\parallel}^{(0)}) + g_z^{(1)}\right]z\right\} \right) \times \exp\left[i\left(\mathbf{K}_{\parallel}^{(0)} + \mathbf{g}_{\parallel}^{(1)}\right) \cdot \mathbf{R}\right] = \sum_{g^{(1)}} A_{g^{(1)}}^{(1)}(\mathbf{K}_{\parallel}^{(0)}, z) \exp\left[i\left(\mathbf{K}_{\parallel}^{(0)} + \mathbf{g}_{\parallel}^{(1)}\right) \cdot \mathbf{R}\right]. \quad (5)$$

Thus, considering the transmission waves from the first layer at $z = z_1$ to be the partial incident waves for the second layer, as shown in Fig. 1, the incident wavefunction for the second layer can be written using equation (5) as

$$\Psi_{\text{inci}}^{(1) \rightarrow (2)}(\mathbf{R}, z_1) \equiv \sum_{g^{(1)}} A_{g^{(1)}}^{(1)}(\mathbf{K}_{\parallel}^{(0)}, z_1) \exp\left[i\left(\mathbf{K}_{\parallel}^{(0)} + \mathbf{g}_{\parallel}^{(1)}\right) \cdot \mathbf{R}\right]. \quad (6)$$

It should be noted that the transverse vector of the incident direction $\mathbf{K}_{\parallel}^{(0)}$ for the first layer changes to $\mathbf{K}_{\parallel}^{(0)} + \mathbf{g}_{\parallel}^{(1)}$ for the second layer due to Bragg reflection $\mathbf{g}^{(1)}$, as shown in Fig. 1, and the complex amplitudes $A_{g^{(1)}}^{(1)}(\mathbf{K}_{\parallel}^{(0)}, z_1)$ correspond to the

amplitudes for each partial incident wave. Therefore, the wavefunction in the second layer is given as

$$\begin{aligned} \Psi^{(2)}(\mathbf{R}, z) = & \sum_{g^{(1)}} \sum_{g^{(2)}} \sum_j \alpha^{(2),j}(\mathbf{K}_{\parallel}^{(0)} + \mathbf{g}_{\parallel}^{(1)}) C_{g^{(2)}}^{(2),j}(\mathbf{K}_{\parallel}^{(0)} + \mathbf{g}_{\parallel}^{(1)}) \\ & \times \exp\left[i\left(\mathbf{K}_{\parallel}^{(0)} + \mathbf{g}_{\parallel}^{(1)} + \mathbf{g}_{\parallel}^{(2)}\right) \cdot \mathbf{R}\right] \\ & \times \exp\left\{i\left[k_z^{(2)}(\mathbf{K}_{\parallel}^{(0)} + \mathbf{g}_{\parallel}^{(1)}) + \gamma^{(2),j}(\mathbf{K}_{\parallel}^{(0)} + \mathbf{g}_{\parallel}^{(1)})\right.\right. \\ & \left.\left.+ g_z^{(2)}\right]z\right\}. \end{aligned} \quad (7)$$

It should be noted that this wavefunction is calculated using only the Bragg reflections $\mathbf{g}^{(2)}$ excited by the inherent unit cell in the second layer. The excitation amplitudes for the Bloch states are calculated from the boundary condition in the same manner as that for the first layer:

$$\begin{bmatrix} \alpha^{(2),1}(\mathbf{K}_{\parallel}^{(0)} + \mathbf{g}_{\parallel}^{(1)}) \\ \alpha^{(2),2}(\mathbf{K}_{\parallel}^{(0)} + \mathbf{g}_{\parallel}^{(1)}) \\ \alpha^{(2),3}(\mathbf{K}_{\parallel}^{(0)} + \mathbf{g}_{\parallel}^{(1)}) \\ \vdots \end{bmatrix} = \left[\tilde{\mathbf{C}}^{(2)}(\mathbf{K}_{\parallel}^{(0)} + \mathbf{g}_{\parallel}^{(1)})\right]^{-1} \cdot \begin{bmatrix} A_{g^{(1)}}^{(1)}(\mathbf{K}_{\parallel}^{(0)}, z_1) \\ 0 \\ 0 \\ \vdots \end{bmatrix}, \quad (8)$$

where $A_{g^{(1)}}^{(1)}(\mathbf{K}_{\parallel}^{(0)}, z_1)$ is the complex amplitude of a partial incident wave at the entrance boundary. All excitations must be calculated for every $\mathbf{g}_{\parallel}^{(1)}$. The incident wave for the third layer at $z = z_2$ is written from the transformation of equation (5) as

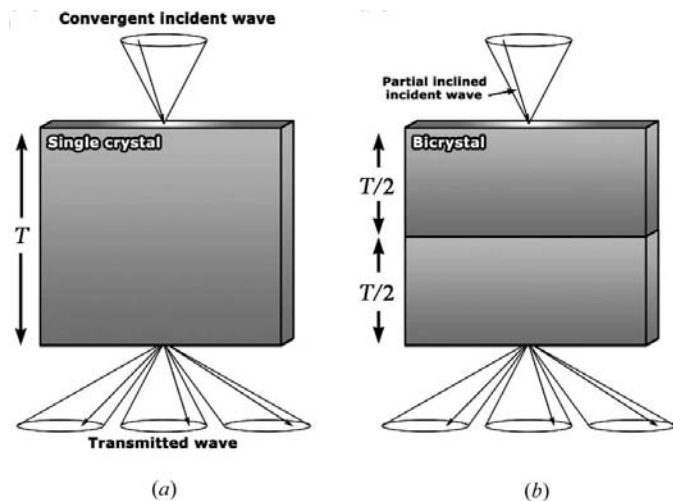


Figure 2 Schematic diagrams of the samples used in the convergence test of our method. (a) The single-layer structure used in the conventional dynamical simulation and (b) the two-layered structure used in the dynamical simulation with both layers having the same thickness.

$$\begin{aligned} \Psi^{(2)}(\mathbf{R}, z_2) = & \sum_{g^{(1)}} \sum_{g^{(2)}} \left(\sum_j \alpha^{(2),j}(\mathbf{K}_{\parallel}^{(0)} + \mathbf{g}_{\parallel}^{(1)}) C_{g^{(2)}}^{(2),j}(\mathbf{K}_{\parallel}^{(0)} + \mathbf{g}_{\parallel}^{(1)}) \right. \\ & \times \exp\left\{i\left[k_z^{(2)}(\mathbf{K}_{\parallel}^{(0)} + \mathbf{g}_{\parallel}^{(1)}) + \gamma^{(2),j}(\mathbf{K}_{\parallel}^{(0)} + \mathbf{g}_{\parallel}^{(1)})\right.\right. \\ & \left.\left.+ g_z^{(2)}\right]z_2\right\} \exp\left[i\left(\mathbf{K}_{\parallel}^{(0)} + \mathbf{g}_{\parallel}^{(1)} + \mathbf{g}_{\parallel}^{(2)}\right) \cdot \mathbf{R}\right] \\ = & \sum_{g^{(1)}} \sum_{g^{(2)}} A_{g^{(1)}}^{(1)}(\mathbf{K}_{\parallel}^{(0)}, z_1) A_{g^{(2)}}^{(2)}(\mathbf{K}_{\parallel}^{(0)} + \mathbf{g}_{\parallel}^{(1)}, z_2) \\ & \times \exp\left[i\left(\mathbf{K}_{\parallel}^{(0)} + \mathbf{g}_{\parallel}^{(1)} + \mathbf{g}_{\parallel}^{(2)}\right) \cdot \mathbf{R}\right] \\ \equiv & \Psi_{\text{inci}}^{(2) \rightarrow (3)}(\mathbf{R}, z_2). \end{aligned} \quad (9)$$

Repeating the same calculation explained above, the transmitted waves through n layers are written as

$$\begin{aligned} \Psi^{\text{trans}}(\mathbf{R}, \mathbf{K}_{\parallel}^{(0)}) = & \sum_{g^{(1)}} \sum_{g^{(2)}} \dots \sum_{g^{(n)}} T_{g^{(1)+g^{(2)}+\dots+g^{(n)}} \\ & \times \exp\left[i\left(\mathbf{K}_{\parallel}^{(0)} + \mathbf{g}_{\parallel}^{(1)} + \mathbf{g}_{\parallel}^{(2)} + \dots + \mathbf{g}_{\parallel}^{(n)}\right) \cdot \mathbf{R}\right], \end{aligned} \quad (10)$$

where the transmission coefficients are expressed as

$$\begin{aligned} T_{g^{(1)+g^{(2)}+\dots+g^{(n)}} = & \exp\left[-ik_z^{(0)}(\mathbf{K}_{\parallel}^{(0)})z_n\right] \\ & \times \sum_{g^{(1)}} \sum_{g^{(2)}} \dots \sum_{g^{(n)}} A_{g^{(1)}}^{(1)}(\mathbf{K}_{\parallel}^{(0)}, z_1) A_{g^{(2)}}^{(2)}(\mathbf{K}_{\parallel}^{(0)} + \mathbf{g}_{\parallel}^{(1)}, z_2) \\ & \times \dots \times A_{g^{(n)}}^{(n)}(\mathbf{K}_{\parallel}^{(0)} + \mathbf{g}_{\parallel}^{(1)} + \dots + \mathbf{g}_{\parallel}^{(n)}, z_n). \end{aligned} \quad (11)$$

In this manner, waves transmitted through a multilayer structure can be obtained. Because a superlattice cell is not required in this calculation, the number of waves in an eigenvalue calculation is equal to the number of diffracted waves excited by each unit cell. In other words, it is not necessary to consider the waves excited by other unit cells and double diffraction. Thus, the processing time required for each eigenvalue calculation is less than that required for the calculation in the conventional layer-by-layer method with a superlattice cell. However, the number of eigenvalue calculations increases on considering partial incident waves. Although this is a disadvantage, this method enables us to carry out practical calculations for coincident lattices as well as incommensurate lattices. Therefore, this method provides a new and efficient way for quantitative analysis of a lattice-mismatch system using TEM with dynamical simulation based on the Bloch-wave method. It should be noted that this method can be applied to convergent-beam electron diffraction (CBED) and high-angle annular dark field (HAADF) scanning transmission electron microscopy (STEM) simulations without any problem.

3. Results and discussion

3.1. Evaluation from zeroth-order Laue zone CBED patterns

First, whether or not our method yields an appropriate result for various incidence azimuths is investigated by using

zeroth-order Laue zone (ZOLZ) CBED patterns for two cases. In the first case, typical CBED calculations are performed for a single Si(011) crystal, as shown in Fig. 2(a). In the second case, the single crystal is first divided into two layers of equal thickness, as shown in Fig. 2(b), and then our method is applied. On the basis of the convergence test carried out at 100 kV, 129 ZOLZ reflections were used in each dynamical simulation. The corresponding simulated ZOLZ CBED patterns at two thicknesses obtained by using typical conventional dynamical simulation and our method are shown in Figs. 3(a, d) and 3(b, e), respectively, where images on a logarithmic scale are inserted in the upper right-hand quarter. For a more detailed comparison, rocking curves of (000), (200) and (400) discs are shown in Figs. 3(c) and 3(f). It is found that our method and the usual calculation yield the same results for each thickness.

3.2. Comparison of HRTEM images using a superlattice cell

Whether our method yields an appropriate result for a highly epitaxial thin film on a substrate was examined by using a system of epitaxial Al(100) on GaAs(100). Here it is assumed that all Al atoms are projected onto Ga and As sites, as illustrated in Fig. 4(a). Fig. 4(b) indicates the corresponding diffraction pattern. The thickness of the Al and GaAs layers was equal, as shown in Fig. 4(c). Figs. 5(a) and 5(b) show the

simulated wavefields of epitaxial Al on GaAs plotted against the thickness by using our method and the conventional method with a superlattice cell, respectively. In the superlattice method 293 ZOLZ reflections were used at 200 kV, while in our method 145 ZOLZ reflections were used for the Al layer and 293 for the GaAs layer, which are sufficient to obtain the exact Bloch waves. It is found that there is no difference between the two calculations. To further confirm this result, a few intensities for transmission coefficients against thickness calculated by our method and the conventional method are shown in Fig. 5(c). The summation of all diffracted intensities as well as (000), (020)_{Al}/(220)_{GaAs} and (220)_{Al}/(400)_{GaAs} components calculated by our method agree perfectly with those calculated by using the superlattice cell, thus confirming the validity of our method.

3.3. Simulations of CdSe clusters embedded in MgO

Here, a CdSe cluster embedded in MgO was regarded as a three-layered structure comprising 10 nm-thick wurtzite structured CdSe with lattice parameters $a = 4.298$ and $c = 7.002$ Å sandwiched between 5 nm-thick rock-salt structured MgO with lattice parameter $a = 4.213$ Å. The simulated HRTEM image is shown in Fig. 6(a), where the acceleration voltage is set to 200 kV, the spherical aberration coefficient C_s is 1 mm, the defocus value Δf is -50 nm, the objective aper-

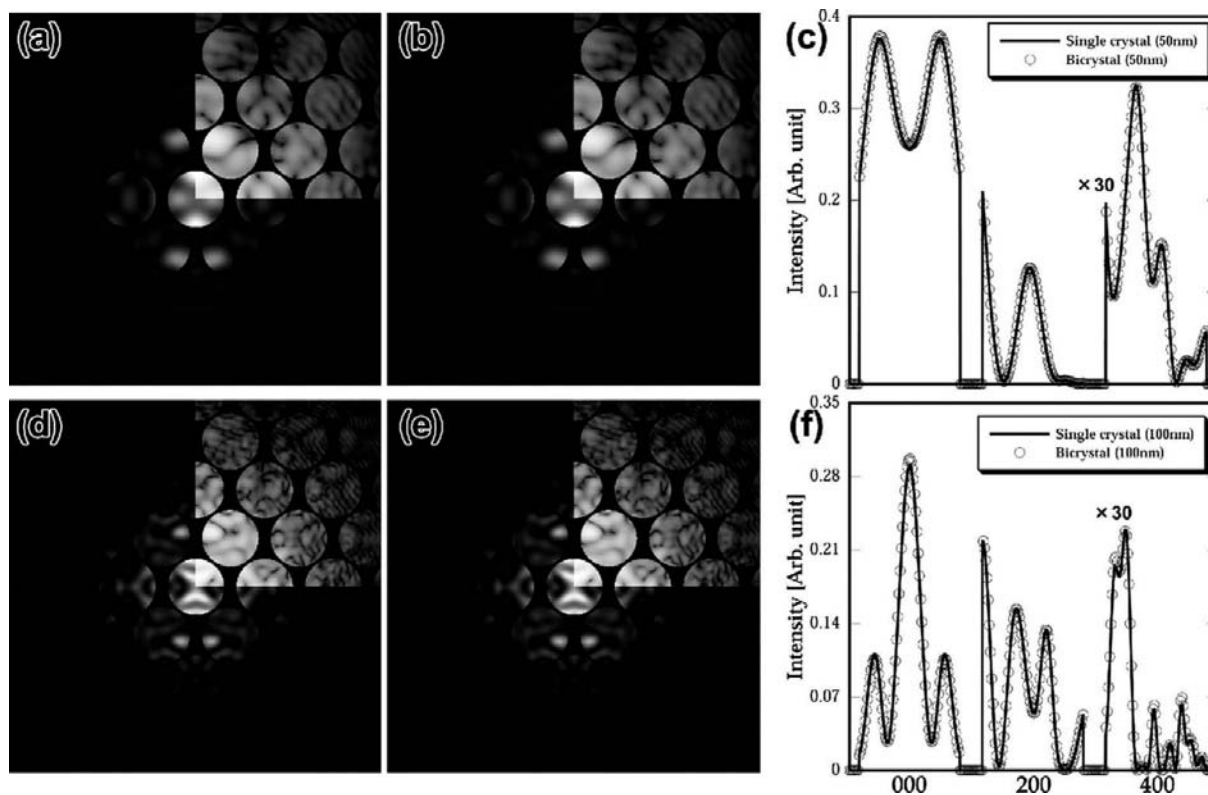


Figure 3 (a, b) Simulated CBED patterns of a 50 nm-thick [011]-oriented Si crystal using conventional dynamical simulation and our method, respectively. (c) Rocking curves of (000), (200) and (400) discs along the [200] direction. (d–f) Same as (a–c) except that a 100 nm-thick [011]-oriented Si crystal is used. The images displayed on a logarithmic scale are shown in the upper right-hand quarter of parts (a), (b), (d) and (e).

ture size is 20 mrad, the defocus spread Δ is 2 nm and the illumination semi-angle α is 0.6 mrad. $[\bar{1}\bar{2}10]_{\text{CdSe}}$ is parallel to $[010]_{\text{MgO}}$, and $[000\bar{1}]_{\text{CdSe}}$ is parallel to $[001]_{\text{MgO}}$. In the simulation, 57 ZOLZ reflections were used in the MgO layer and 191 reflections were used in the CdSe layer. Our method requires a superlattice cell for a practical cluster calculation. However, different superlattice cells (or unit cells) can be selected for upper and lower layers, which is different to the conventional method.

Fig. 6(a) exhibits a set of characteristic bright lines along the $[010]_{\text{MgO}}$ direction. The pattern of the bright lines changes in a complex way depending on the position, hereafter called ‘moiré-like fringes’. The moiré-like fringes may be regarded as the moiré fringes at an atomic resolution. For ease of viewing, the representative positions of the moiré-like fringes are

indicated by the black arrows and lines in Fig. 6(a). When two thin crystal layers overlap and are rotated by a few degrees or when their lattice constants differ, a pattern of interference fringes is observed. These are known as moiré fringes and were first reported on graphite lamellae by Mitsuishi *et al.* (1951). For a two-layer system with different lattice constants and a parallel orientation, the pattern is considered to be generated due to double diffraction (Reimer, 1989). The moiré fringes have a common period that is independent of the position, which is different to the moiré-like fringes. In order to observe the moiré-like fringes in detail, enlarged HRTEM images of regions A, B and C indicated in Fig. 6(a) are shown in the left-hand side of Fig. 6(b). The moiré-like fringes commonly run along the $[010]_{\text{MgO}}$ direction; however, the number of bright lines and their spacing changes significantly depending on the position.

The moiré-like fringes appear to be related to the relative shift of the two crystals. This fact is inferred from comparing the bright lines shown in Fig. 6(a) with the corresponding projected potentials and schematic relative shifts shown in Fig. 6(b). In other words, the relative lattice shift between an epitaxial film and a substrate or embedded clusters and a host crystalline matrix may be estimated by the moiré-like fringes through comparison of the experi-

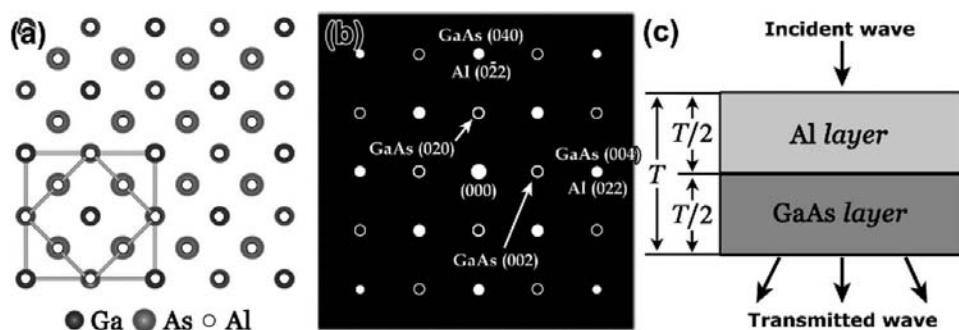


Figure 4

(a) Schematic projected atomic positions, (b) electron-diffraction pattern for epitaxial Al(100) on GaAs(100) and (c) schematic diagram of the Al/GaAs multilayer structure for dynamical simulations.

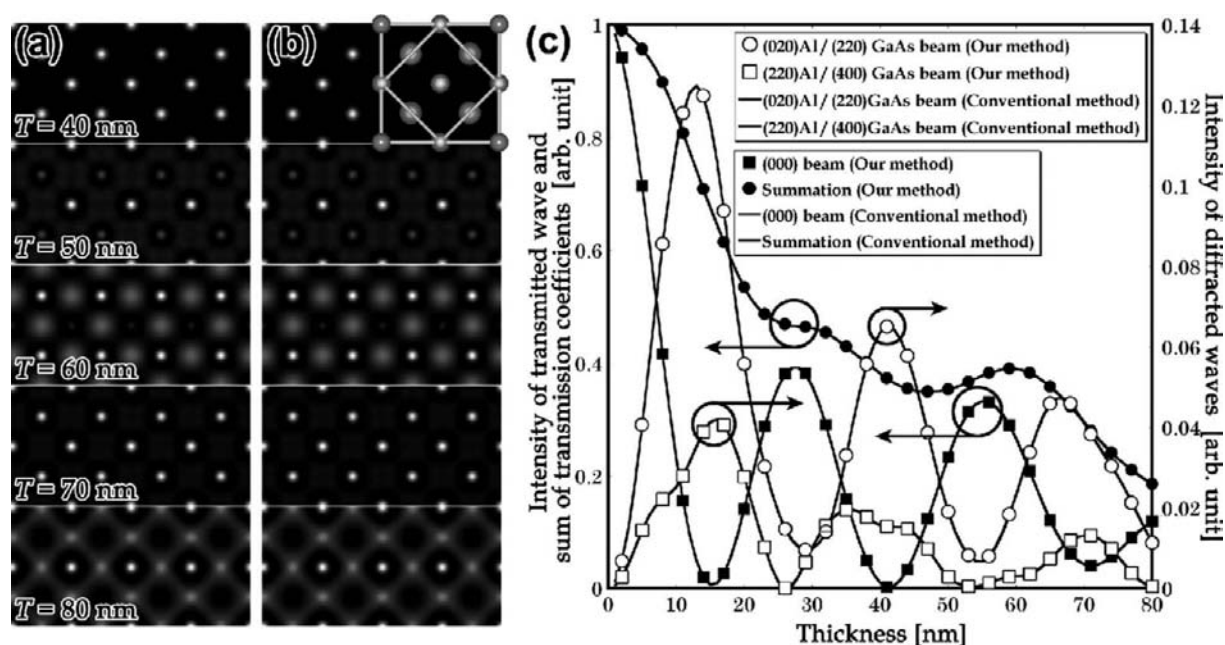


Figure 5

Comparison of through-thickness simulated exit wavefields for a two-layered system of epitaxial Al(100) on GaAs(100) with both layers having equal thickness calculated by (a) our method and (b) with a superlattice. The schematic diagram of the superlattice cell is shown at the top right of (b). (c) Comparison of each transmitted wave intensity and the summation of all diffracted intensities as a function of thickness calculated by our method and with a superlattice. The arrows show which vertical axis is to be chosen.

mental HRTEM images and the corresponding simulations based on our method, since clear moiré-like fringes have been reported in highly epitaxial thin films on substrates (Jiang *et al.*, 2007) and embedded nanocrystals (Donnelly & Rossouw, 1985, 1986; van Huis *et al.*, 2004a,b).

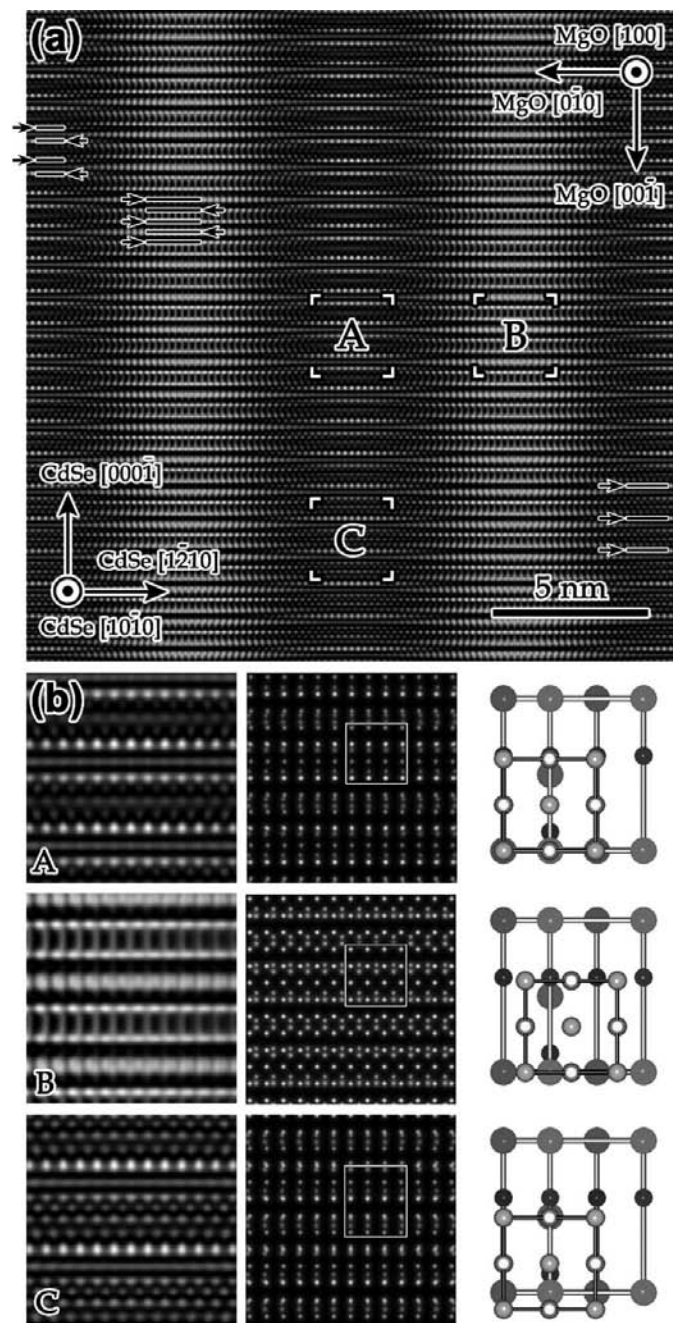


Figure 6 (a) Simulated HRTEM image of the three-layered structure comprising 10 nm-thick [10 $\bar{1}$ 0]-oriented wurtzite-structured CdSe sandwiched between 5 nm-thick [100]-oriented rock-salt-structured MgO. (b) Left: enlarged HRTEM images of regions A, B and C indicated by the white squares in (a). Center: the corresponding projected potential images. Right: the corresponding relative shift of the lattice planes.

4. Summary

A different dynamical theory for plan-view HRTEM for multilayer systems without the limitation of a superlattice cell is proposed. The accuracy of our method is clarified by comparing CBED calculations of Si(011) and HRTEM calculations of a system of epitaxial Al(100) on GaAs(100). This method enables us to make a quantitative comparison between the experimental and simulated HRTEM images for a cluster (with a lattice mismatch) embedded in a host crystalline matrix and heteroepitaxial growth of lattice-mismatched systems. Furthermore, simulations using this method revealed that moiré-like fringes are formed due to the relative shift of the crystal-lattice planes. This method can also be applied to CBED and HAADF STEM simulations without any problem.

References

Al-Khafaji, M. A., Cherns, D., Rossouw, C. J. & Woolf, D. A. (1992). *Philos. Mag. B*, **65**, 385–399.
 Bethe, H. A. (1928). *Ann. Phys.* **87**, 55–129.
 Cowley, J. M. & Moodie, A. F. (1957). *Acta Cryst.* **10**, 609–619.
 Donnelly, S. E. & Rossouw, C. J. (1985). *Science*, **230**, 1272–1273.
 Donnelly, S. E. & Rossouw, C. J. (1986). *Nucl. Instrum. Methods B*, **13**, 485–489.
 Eaglesham, D. J., Kiely, C. J., Cherns, D. & Missous, M. (1989). *Philos. Mag. A*, **60**, 161–175.
 Fujimoto, F. (1959). *J. Phys. Soc. Jpn*, **14**, 1558–1568.
 Gao, H.-J., Chen, C. L., Rafferty, B., Pennycook, S. J., Luo, G. P. & Chu, C. W. (1999). *Appl. Phys. Lett.* **75**, 2542–2544.
 Hirsch, P. B., Howie, A., Nicholson, P. B., Pashley, D. W. & Whelan, M. J. (1965). *Electron Microscopy of Thin Crystals*. London: Butterworths.
 Huis, M. H. van, van Veen, A., Schut, H., Eijt, W. H., Kooi, B. J. & DeHosson, J. Th. M. (2004a). *Nucl. Instrum. Methods B*, **216**, 121–126.
 Huis, M. H. van, van Veen, A., Schut, H., Eijt, W. H., Kooi, B. J. & DeHosson, J. Th. M. (2004b). *Nucl. Instrum. Methods B*, **218**, 410–415.
 Hull, R., Ourmaz, A., Rau, W. D., Schwander, P., Green, M. L. & Tung, T. R. (2000). *Handbook of Semiconductors*. New York: Wiley-VCH.
 Ishizuka, K. (1982). *Acta Cryst.* **A38**, 773–779.
 Jia, C. L., Lentzen, M. & Urban, K. (2003). *Science*, **299**, 870–873.
 Jia, C. L. & Urban, K. (1999). *Philos. Mag. Lett.* **79**, 859–867.
 Jiang, J. C., Meletis, E. I., Yuan, Z. & Chen, C. L. (2007). *Appl. Phys. Lett.* **90**, 051904.
 Mitsuishi, T., Nagasaki, H. & Ueda, R. (1951). *Proc. Imp. Acad. Jpn*, **27**, 86.
 Reimer, L. (1989). *Transmission Electron Microscopy*. Berlin: Springer-Verlag.
 Rossouw, C. J., Al-Khafaji, M., Cherns, D., Steeds, J. M. & Touaitia, R. (1991). *Ultramicroscopy*, **35**, 229–236.
 Rossouw, C. J. & Perovic, D. D. (1993). *Ultramicroscopy*, **48**, 49–61.
 Self, P. G. (1982). *J. Microsc.* **127**, 293–299.
 Timp, G. (1988). *Technical Digest*. San Francisco: IDEM.
 Van Dyck, D. (1980). *J. Microsc.* **119**, 141.
 Wang, S. Q., Peng, L.-M., Duan, X. F. & Chu, Y. M. (1992). *Ultramicroscopy*, **45**, 405–409.
 Yamazaki, T., Watanabe, K., Kuramochi, K. & Hashimoto, I. (2006). *Acta Cryst.* **A62**, 233–236.